Real-time forecast service for geomagnetically induced currents

ESA/ESTEC Contract No. 16953/02/NL/LvH

WP 400 Technical Note
Forecasting local geomagnetic field fluctuations and GIC from
solar wind data

P. Wintoft and M. Wik
Swedish Institute of Space Physics

27 February 2005

Document status sheet

ISSUE	REVISION	DATE	REASON FOR CHANGE
0	0	26 April 2004	First draft.
0	1	5 October 2004	Most sections updated.
0	2	27 February 2005	Most sections updated.

Summary

This document describes the models that will produce forecasts of the rate-of-change of the horizontal components of the local geomagnetic field in South Sweden based on ACE real time solar wind data. Both the north-south (ΔX) and east-west (ΔY) directions are considered.

It is clear that predicting $\Delta H = (\Delta X, \Delta Y)$ with one minute resolution is with current knowledge impossible. Therefore, we motivate the use of temporal root-mean-square (RMS) ΔH formed over 10 minute intervals. A resolution of 10 minutes has been found to be a good trade off between high resolution and accurate forecasts. The optimal forecast lead time is 30 minutes and the correlation between model output and observed log RMS ΔH is approximately 0.80. The models forecast the 10-minute RMS ΔX and ΔY at Brorfelde (BFE: 11.67°E, 55.63°N),Denmark, and Uppsala (UPS: 17.35°E, 59.90°N), Sweden.

The magnetic field variations ΔH is interpolated over a dense grid covering South Sweden using an equivalent ionospheric current model. Based on the interpolated ΔH the electric field and thus the geomagnetic induced currents may be calculated for any given location. We show that the interpolated 10-minute RMS ΔH may be estimated from the two locations BFE and UPS. Therefore, the prediction model can be generalised to arbitrary locations.

Finally, we provide a linear model relating RMS ΔH at Brorfelde, Denmark, and Uppsala, Sweden, to RMS GIC at a single location. There is also a close linear relation between RMS GIC and MAX GIC, where the latter is the maximum GIC in a 10 minute interval. This is useful as an estimate of the maximum GIC that will occur.

Abbreviations and symbols

ACE Advanced Composition Explorer

ANN Artificial Neural Network

DFT Discrete Fourier Transform

DWT Discrete Wavelet Transform

ETM Exponential Trace Memory

GIC Geomagnetically Induced Current

MODWT Maximum Overlap Discrete Wavelet Transform

TN Technical Note

URD User Requirements Document

WP Work Package

ΔX one minute time difference of the north-south local geomagnetic field
$$\Delta X(t) = X(t+1) - X(t)$$

ΔY one minute time difference of the east-west local geomagnetic field
$$\Delta Y(t) = Y(t+1) - Y(t)$$

ΔH means ΔX and/or ΔY

μ mean

RMS root-mean-square

σ standard deviation

URD matrix

The table below lists the requirements from the URD (*Wintoft et al.*, 2003) together with the relevant sections in this document.

URD req.	Section
CAP.1.	TBD
CAP.2.	TBD
CAP.3.	TBD
CAP.4.	TBD
CAP.5.	TBD
CAP.6.	TBD
CAP.7.	TBD
CAP.8.	TBD
CAP.9.	TBD
CAP.10.	TBD
CAP.11.	TBD
CAP.12.	TBD
CAP.13.	TBD
CAP.14.	TBD
CAP.15.	TBD
CAP.16.	TBD
CON.1.	TBD
CON.2.	TBD
CON.3.	TBD
CON.4.	TBD
CON.5.	TBD

Contents

1 Introduction

This document describes a module for direct solar wind – dH/dt prediction that shall be a part of the GIC Pilot Project. The requirements have been identified in the *User Requirements Document* (*Wintoft et al.*, 2003). The purpose of the project is described in the URD as:

> The space weather refers to conditions on the Sun and in the solar wind, magnetosphere, ionosphere, and thermosphere that can influence the performance and reliability of space-borne and ground-based technological systems, and can endanger human life and health. The space weather can at times induce currents in electrical power grids generally known as GIC (geomagnetically induced currents).
>
> The purpose of this project is to provide a software package that can be used for realtime forecasting of GIC in the Swedish power grid. The software shall be used by power grid operators and tested for a one-year period. During this period, the accuracy and reliability of the software shall be determined, and the usefulness of the software shall be formulated through a cost-benefit analysis. Another aspect is the need to educate the public and decision makers of the potential hazards of GIC and how forecasts can help to mitigate the effects. Thus, the software shall also have a public part.

Our approach to develop a forecast model for GIC is illustrated in Figure 1. With the use of solar wind data and local geomagnetic field data neural networks are trained to predict the root-mean-square (RMS) ΔX and ΔY, or short RMS ΔH. In real time operation only the solar wind data are needed. Based on the forecasted RMS ΔH forecasted GIC may be computed with two different methods. In the first approach, the forecasted RMS ΔH is used as input to a general model for the calculation of GIC (*Viljanen et al.*, 2005). In addition the model also needs the ground conductivity and power grid layout. In the second approach an empirical linear model is developed that predicts the GIC directly from predicted ΔH. It is then possible to explore the difference between the two techniques and to identify the weakest link.

2 The data

A database has been set up as described in the TN of WP 200. Here we make a short summary of the data that are used in this TN.

2.1 Solar wind data

The solar wind plasma and magnetic field data comes in two different temporal resolutions (*Wintoft et al.*, 2004): 16 second sampling of the magnetic field, and 64 second sampling of the plasma. Both the GIC and the geomagnetic data have 60 second resolution. The real-time solar
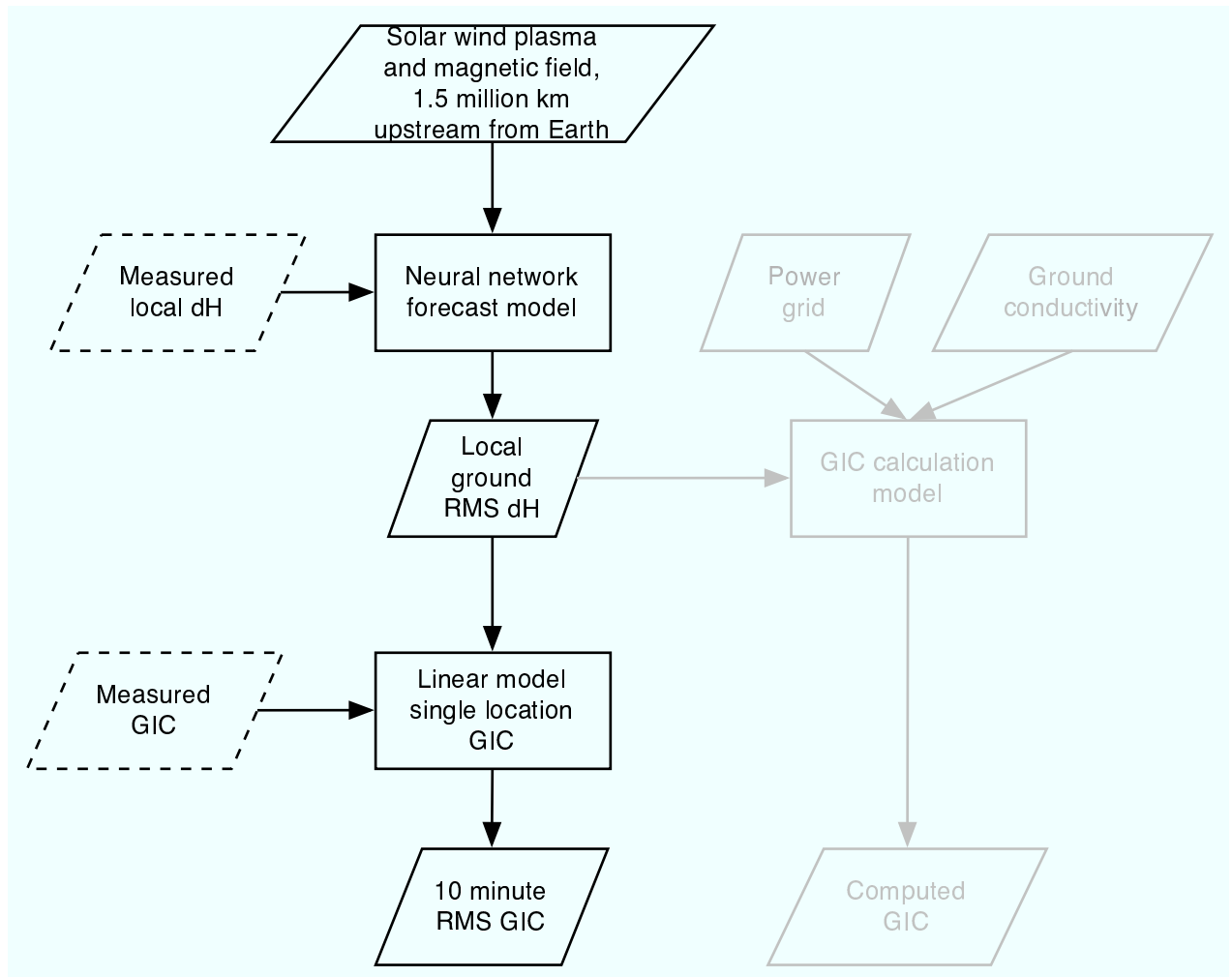
Figure 1: The diagram shows the data flow from the solar wind to the forecasted GIC. The solid boxes represent the part of the model used in real time operation, while the dashed boxes are only necessary during model development. The complete model consists of both parts marked in black and grey. This document addresses the part in black.

wind data at SEC[1] are also given with 60 second resolution, where the plasma data have been resampled from 64 seconds to 60 seconds. However, resampling the data introduces artificial frequencies that result in differences between longer temporal averages formed from the 64- and 60-second time series. E.g., forming 5-minute averages from the 64- and 60-second data may result in occasional differences of more than 8 cm^{-3} in the density and more than 20 km/s in the velocity. Thus, resampling the data from 64 seconds to 60 seconds should be avoided for the analysis and model development.

2.2   Local geomagnetic field

We select observed geomagnetic from Brorfelde (11.67°E,55.63°N) and Uppsala (17.35°E,59.90°N) as these sites are closest to the region of Sweden we currently shall study. As stated in WP 300 (*Viljanen et al.*, 2005) the prime quantity to use when calculating GIC is the time derivatives of the horizontal magnetic field components dX/dt and dY/dt. The derivatives are approximated using the forward difference

$$\Delta X(t) = X(t+1) - X(t), \tag{1}$$

where t is in minutes and X is the north-south horizontal magnetic field component. Similarly we have

$$\Delta Y(t) = Y(t+1) - Y(t), \tag{2}$$

east-west component.

2.3   Interpolated geomagnetic field in a dense grid

The method to interpolate the geomagnetic field in a dense grid over South Sweden in described in *Viljanen et al.* (2005). The interpolated data consist of the magnetic field components (X, Y) with one minute resolution equidistantly distributed in 1° steps in longitude from 11° to 18°, and in 0.5° steps in latitude from 55° to 60°, giving in total $8 \times 11 = 88$ points.

2.4   GIC data

The recorded GIC data covers three periods: 1998-09-17 – 10-28, 1999-08-15 – 11-14, and 2000-01-22 – 08-13. The first period has very few data gaps, while for the last two periods it has been stated that data has only been collected when GIC> 1 Ampere.

---

[1] http://www.sec.noaa.gov/ftpdir/lists/ace/

3 Analysis

3.1 A case study – September 1998

On 24 September 1998 the Earth's magnetosphere was hit by a strong solar wind shock with southward magnetic field (Figure 2). The shock reached ACE at L1 at 23:15 UT and about 30 minutes later the effect could be seen in ΔX and ΔY. The increase in ΔX is sudden going from 3 nT/min to the peak value of 54 nT/min in one minute at 23:45 UT. The increase in ΔY is more gradual going from 0 nT/min, through -7, -17, and reaching the peak value after 3 minutes of -41 nT/min at 23:47 UT. The strongest peaks in ΔX and ΔY occur on 25 Sep. around 06:46 with peak values of 123 and 83 nT/min, respectively. There are data gaps in the BFE data at 06:44 and 06:45.
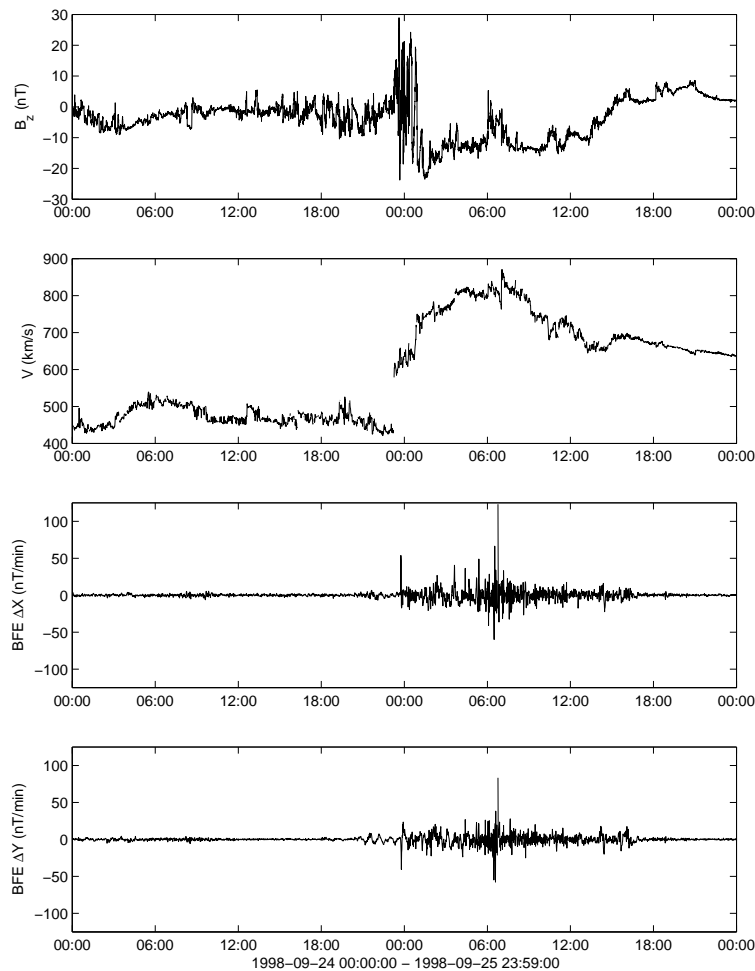

Figure 2: The panels show from top to bottom: solar wind magnetic field component B_z; solar wind velocity V; geomagnetic field fluctuations ΔX at BFE; and geomagnetic field fluctuations ΔY at BFE.

3.2 Auto-correlation

The auto-correlation for $T = 2$-minute average solar wind and ΔX show very different characteristics. The velocity V has an auto-correlation close to 1 for time lags ranging from 0 to 40 minutes. Thus, two measurements of V separated by 40 minutes are most of the time close to equal. Only for occasional shocks there might be a big difference in $V(t)$ and $V(t + 2)$. Similarly, the density n is also highly correlated with a correlation of almost 0.9 at 40 minutes. The magnetic field component B_z has an auto-correlation that drops of quicker, but it is still above 0.6 at 40 minutes lag. Finally, the auto-correlation of ΔX is close to 0 for all time lags, thus it is not possible to predict $\Delta X(t + \tau)$ from $\Delta X(t)$ with a linear model, for any $\tau \geq 2$ minutes.

3.3 Wavelet variance – estimating the spectral density of ΔX and ΔY

Using a discrete wavelet transform (DWT) the ΔX can be decomposed into signals, called details and smooth (or approximation), that are associated with different scales, where the scale corresponds to a wavelength band. The decomposed signals can thus be thought of being a band pass filtered versions of ΔX. The DWT preserves the power in the signal but it is not time invariant, i.e. the DWT of a time shifted ΔX is not equal to the time shifted DWT of ΔX. To ensure time invariance we use a modified DWT, called the Maximum Overlap DWT (MODWT) (*Percival and Walden*, 2002). But with the MODWT the sum of the power of the smooth and details are not equal to the power in ΔX. However, the power is preserved in the wavelet coefficients.

We apply the MODWT using the Daubechies wavelet of order 4 on one-minute ΔX for all data in 1998 resulting in the wavelet coefficients $W_{j,t}$ (details) and V_t (smooth), where the level is $j \in [1, 7]$ and time is $t \in [0, 525599]$. Level j is associated with scale

$$\tau_j = 2^{j-1}. \tag{3}$$

As the time resolution is one minute the scale is also in minutes. The variance, or power, at level j is

$$\nu_j^2 = \sum_t W_{j,t}^2 \tag{4}$$

and the power conservation means that

$$\sum_t \Delta X_t^2 = \sum_j \nu_j^2 + \sum_t V_t^2. \tag{5}$$

The signal at level j is associated with frequencies in the range

$$f_j \in \left[\frac{1}{2^{j+1}}, \frac{1}{2^j} \right] = \left[\frac{1}{4\tau_j}, \frac{1}{2\tau_j} \right]. \tag{6}$$

Thus, if we compute the power spectrum $S(f)$ of ΔX with the Fourier transform then the wavelet variance

$$\nu_j^2 \approx 2 \int_{1/2^{j+1}}^{1/2^j} S(f) df \tag{7}$$

where the factor 2 in front of the integral comes from the fact the $S(f)$ exist for $f \in [-1/2, 1/2]$ and is symmetrical around $f = 0$. In Figure 3 the estimated power spectrum from the MODWT and the DFT are shown (top panel). We see that there is a close agreement between the two estimates. The power in ΔX is concentrated to small scales (high frequencies), which becomes more clear in the two lower panels. The relative power (bottom left panel) is for the first four scales: 32%, 25%, 18%, and 13%. The cumulative relative power (bottom right panel) is 88% using only the wavelet coefficients up to level 4. This is in agreement with our previous conclusion that we need the one-minute data to capture the variance in ΔX. We also see that almost 90% of the signal is found at scales of $\tau_4 = 2^{4-1} = 8$ minutes corresponding to frequencies higher than $1/32$ min^{-1}.
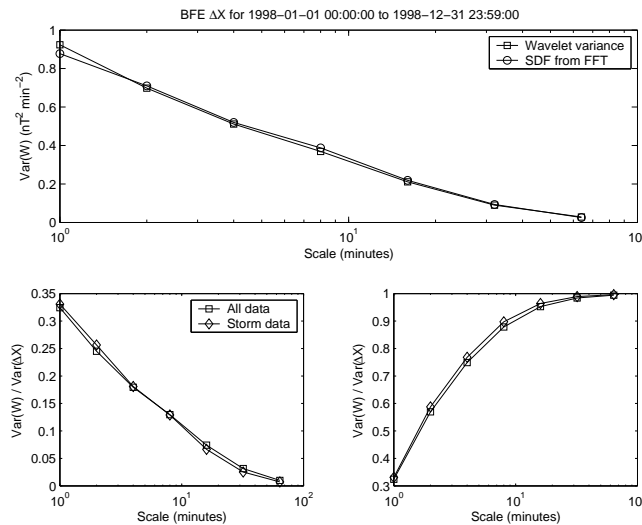

Figure 3: The figure shows the spectral density, or power spectrum, for ΔX normalised with the variance of ΔX. The labels have the following meaning: "All data", all data in 1998; "Storm data", use only one-day periods that contain events where $\Delta X > 20$ nT/min; "SDF from FFT", estimate using a Fourier transform.

We repeat the same analysis for ΔY at Brorfelde, and the result is shown in Figure 4. The spectrum is more flat up to level 4 after which the power decreases rapidly (top panel). The storm time spectrum has a shape similar to the general spectrum (bottom left) and the relative power for the first 4 levels are: 26%, 20%, 19%, and 18%. The four levels together capture 83% of the power and at level 5 it goes over 90% (bottom right).

3.4   Geomagnetic field and GIC

The GIC data consist of measurements of currents flowing through a transformer neutral. The GIC may result from two different sources: space weather induced and non-space weather induced. To explore this we compute the linear correlation between the rate-of-change of the East-West component of the geomagnetic field dX/dt and the GIC. A time lag is introduced
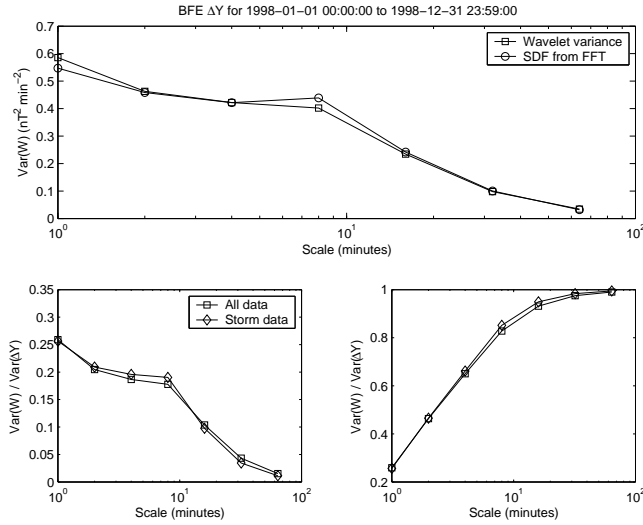
Figure 4: The figure shows the spectral density, or power spectrum, for ΔY normalised with the variance of ΔY. The labels have the following meaning: "All data", all data in 1998; "Storm data", use only one-day periods that contain events where $\Delta Y > 20$ nT/min; "SDF from FFT", estimate using a Fourier transform.

between dX/dt and GIC, and the both unfiltered and filtered GIC are used. For the filtering the DB1 wavelet is used. The wavelet approximation A and detail D are related to the original signal GIC as

$$\text{GIC} = A_1 + D_1 = A_2 + D_2 + D_1 = A_l + \sum_{n=1}^{l} D_n, \tag{8}$$

where l is the level. The filtered GIC at level l is computed as

$$\text{GIC}_l = \begin{cases} \text{GIC} & l = 0 \\ \sum_{n=1}^{l} D_n & l > 0 \end{cases} \tag{9}$$

where D_n is the detail at level l. The signal A_l contains only periods longer than 2^l minutes and thus GIC_l is the high frequency component with periods shorter than 2^l minutes. In Figure 5 we show the correlation between the Brorfelde (BFE) data and the filtered GIC data for the period 1998-09-17 to 1998-10-28. The maximum correlation is reached at a time lag of 2 minutes and filtering level 5. This means that there is a slowly varying component in GIC (period$> 2^5 = 32$ minutes) that is not related to dX/dt. The same analysis is repeated for Upsala (UPS) and the result is shown in Figure 5. The maximum correlation is now found at a time lag of 3 minutes and filtering level 7, corresponding to $2^7 = 128$ minutes.

We now set the filtering level to 6, which corresponds to 64 minutes, and look at the filtered GIC data. Two example periods are shown in Figures 6 and 7. In the top panels are shown a 24-hour interval around 1998-08-25 and 1998-10-18, respectively. In the bottom panels are shown a close-up covering 3 hours. The two examples have quite different characteristics. The first example (Figure 6) contains strong GIC reaching above 50 A. It is difficult to see any difference between the raw GIC and the filtered GIC in the top panel. In the bottom panel
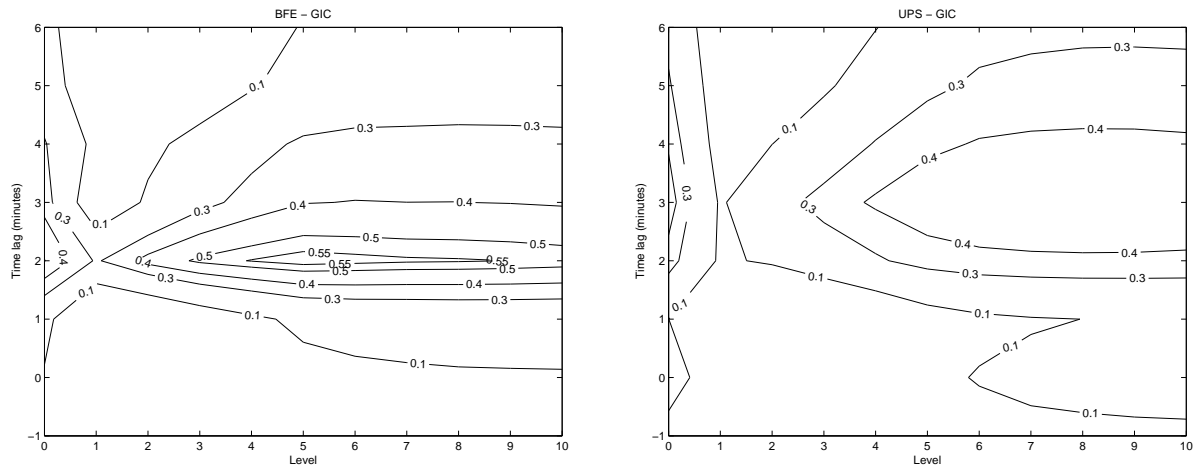
Figure 5: Correlation between dX/dt from Brorfelde (BFE), and Uppsala (UPS), and the GIC data for different levels and time lags. The level is the wavelet filtered GIC data at the corresponding level, where level 0 means unfiltered data.

the differences becomes visible. The second example (Figure 7) is a much calmer period with maximum GIC of 12 A. However, there is a clear bias of 5-6 A in the raw GIC that is removed in the filtered GIC. For the whole period, 1998-09-17 to 1998-10-28, the raw GIC has a mean value of 1.22 A and a standard deviation of 2.2 A, while the filtered GIC has a mean of 0 and a standard deviation of 1.8 A.

The shift of 2 to 3 minutes between the geomagnetic data and the GIC data is at the moment unexplained. It could be due to different time stamping in the different sets. However, it is not crucial in this work as we will use 10 minute data.

The occasional bias term in the GIC is probably related to changes in the power grid configuration affecting the GIC measurements. Again, as we will use 10 minute data, and especially variances of the data, any bias term will be removed in the process. This will be discussed in the next section.

3.5   Time series of RMS ΔX and RMS ΔY

To be able to develop a forecast model of the geomagnetic field the one-minute ΔX and ΔY need to be resampled to a lower time resolution. As already mentioned, any temporal averaging of ΔX is not meaningful because of the weak auto-correlation. Therefore, we will instead study the level of disturbance in ΔX and its relation to the solar wind. In the paper by *Weigel et al.* (2002) models where developed for the coupling from the solar wind to 30 minute averages of the absolute value $|\Delta X|$. However, taking the average of $|\Delta X|$ a large fraction of the variance is lost. Computing the variance of the 30 minute average $|\Delta X|$ and comparing it to the variance
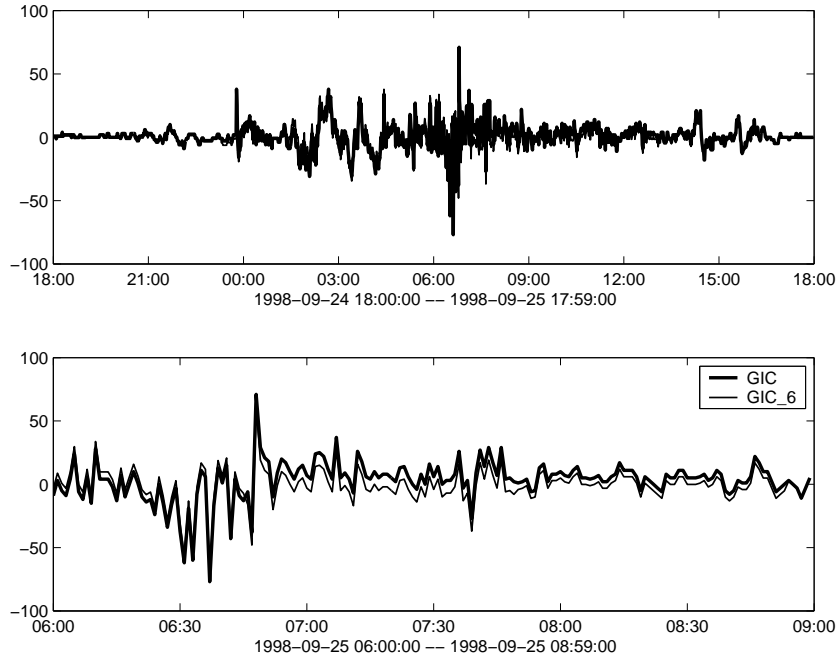
Figure 6: The figure shows the unfiltered (thick line) and filtered (thin line) GIC time series over a 24-hour period (top panel) during 24–25 Sep. 1998. An enlarged part is shown in the bottom panel covering three hours.

of ΔX we get

$$\frac{\text{VAR}(\langle|\Delta X|\rangle)}{\text{VAR}(\Delta X)} = 0.35 \tag{10}$$

which means that only about 35% of the variance is captured. Decreasing to 10 minute averages the fraction increases to 42%. The low explained variance is an effect of that most of the power in ΔX is located at small scales as found from the wavelet analysis. To improve on the situation we may instead form 10-minute root-mean-square of ΔX and the explained variance now increases to

$$\frac{\text{VAR}(\text{RMS}\Delta X)}{\text{VAR}(\Delta X)} = 0.65. \tag{11}$$

Another interesting feature with RMS, or MS, is that it is related to the variance of the wavelet coefficients via Equation 5.

4 Forecast models of RMS ΔX and RMS ΔY using neural networks

Here we describe the neural network model for the prediction of the 10-minute RMS ΔX and ΔY at Brorfelde and Uppsala.
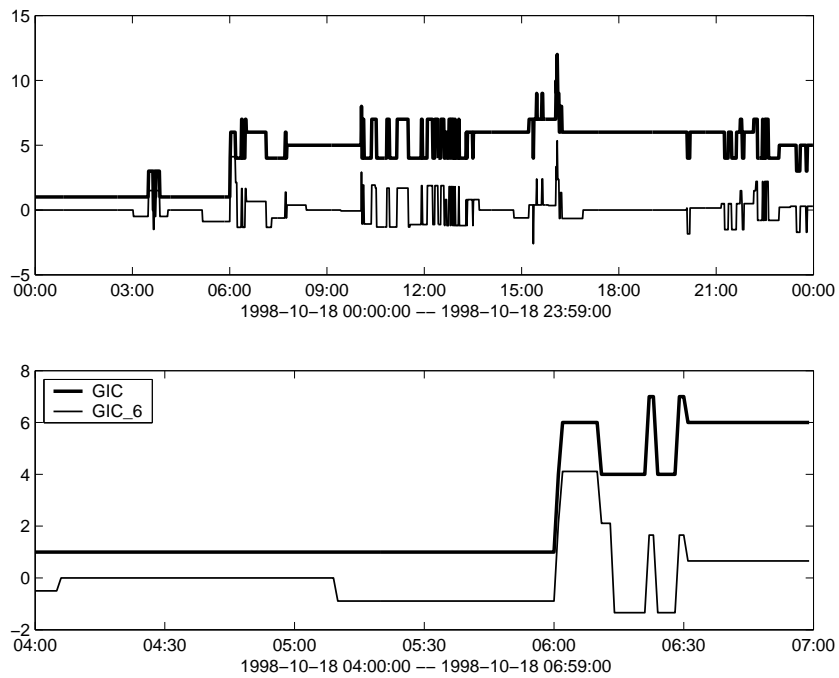
Figure 7: The figure shows the unfiltered (thick line) and filtered (thin line) GIC time series over a 24-hour period (top panel) in 18 Oct. 1998. An enlarged part is shown in the bottom panel covering three hours.

4.1   10-minute resolution data

As described in Section 4.2 we will use data with 10 minute resolution in the forecast model. First we have the 10-minute average as

$$\mu(s) = \frac{1}{10} \sum_{t=10s}^{10s+9} x(t).$$
(12)

The average captures quite well the dynamics in the solar wind. Another quantity that is interesting is the standard deviation

$$\sigma(s) = \sqrt{\frac{1}{9} \sum_{t=10s}^{10s+9} (x(t) - \mu(s))^2}$$
(13)

as this is related to turbulence and strong gradients that are not seen in the average. Finally, we also have the root-mean-square (RMS) value

$$r(s) = \sqrt{\frac{1}{10} \sum_{t=10s}^{10s+9} x^2(t)}$$
(14)

which is related to the power in the signal. The solar wind data are resampled using the average and standard deviation where $x(t)$ is replaced by B_z, n, and V. The rate-of-change of the local geomagnetic field is resampled using the RMS where $x(t)$ is replaced with ΔX and ΔY at Uppsala and Brorfelde.

4.2   Temporal averages and the relation to prediction lead time

Assume we have a variable $x(t)$ that is collected with a sampling interval Δt resulting in the time series x_i. The corresponding time stamp t_i marks the beginning of the interval so that x_i is the average of $x(t)$ over the interval $t \in [t_i, t_{i+1}]$ where $t_{i+1} = t_i + \Delta t$. Similarly, we may have another variable $y(t)$ sampled to y_i. If we now wish to develop a model that predicts y from x with some lead time τ we have $\hat{y}(t + \tau) = f(x(t))$, where $\hat{y}$ is the prediction of y. This leads to the discrete model

$$\hat{y}_{i+n} = f(x_i)$$
(15)

where $\tau = n\Delta t$.

To understand the true forecast time assume that the current time is t_0. The latest input is x_{-1} that has been collected over the time interval $[t_{-1}, t_0]$. With a forecast time of $\tau = n\Delta t$ we will thus be forecasting y_{n-1} resulting in a true forecast time of $\tau' = \tau - \Delta t$. In order for the model to perform actual forecasts we must have $\Delta t \leq \tau$.

In the case of solar wind – magnetosphere coupling, part of the lead time is associated with the solar wind travel time from L1 to Earth. In Figure 8 the travel time is shown for velocities in the range $[300, 1000]$ km/s. If we only consider velocities up to 830 km/s then it is possible

to make forecasts of 30 minutes. The ACE 2-minute average velocity exceeds 830 km/s in 27 events for the period 1998 to current, and the maximum velocity is 980 km/s corresponding to a travel time of 25 minutes. Thus, using a 30 minutes forecast lead time will capture most of the events, and for higher velocities the lead time will be shifted by mostly 5 minutes.
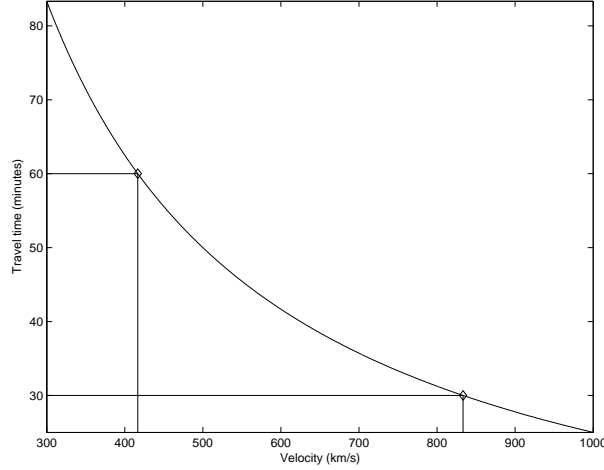

Figure 8: The figure shows the prediction lead time as a function of velocity as measured at L1. The straight lines marks the velocities at lead times of 30 and 60 minutes, respectively.

The ACE spacecraft is not located exactly on the Sun-Earth line but is on an orbit around L1. Therefore, the spacecraft does not measure the solar wind directly upstream from the Earth which will introduce uncertainties on the time of arrival and evolution of solar wind structures. Temporal averaging will reduce the uncertainties and a resolution of $\Delta t = 10$ minutes is a good trade-off leading to a true forecast time of $30 - 10 = 20$ minutes.

4.3   Architecture

The neural network takes solar wind data and time as input and predicts the $\log r$. Four different models are developed that predicts $r_{X,BFE}$, $r_{Y,BFE}$, $r_{X,UPS}$, and $r_{Y,UPS}$, respectively. The inputs are 10 minute averages and standard deviations. The inputs are collected into the input vector

$$\mathbf{X} = [d_1, d_2, l_1, l_2, \mu_{Bz}, \sigma_{Bz}, \mu_n, \sigma_n, \mu_V, \sigma_V] = [X_1, \ldots, X_{10}], \tag{16}$$

where

$$[d_1, d_2] = \left[\sin \frac{2\pi \mathrm{DOY}}{365}, \cos \frac{2\pi \mathrm{DOY}}{365}\right] \tag{17}$$

are the sine and cosine of the day-of-year (DOY),

$$[l_1, l_2] = \left[\sin \frac{2\pi \mathrm{LT}}{24}, \cos \frac{2\pi \mathrm{LT}}{24}\right] \tag{18}$$

are the sine and cosine of the local time (LT), and the $\mu_\bullet$ and $\sigma_\bullet$ are the mean and standard deviation of the solar wind data. The inputs are then normalised according to

$$x_i = \frac{X_i - a_i}{b_i} \tag{19}$$

where

$$\mathbf{a} = [0, 0, 0, 0, 0, 0.92, 8.0, 0.61, 490, 4.6] \tag{20}$$
$$\mathbf{b} = [2.1, 2.1, 2.1, 2.1, 18, 3.6, 24, 3.1, 320, 15]. \tag{21}$$

The normalisation constants have been chosen so that the mean of x_i is approximately 0, and the standard deviation is approximately 0.3. The neural network can now be written as

$$\hat{y}(t + \tau) = f(\mathbf{x}(t), N_H) \tag{22}$$

where τ is the prediction time, N_H the number of hidden neurons, and $\hat{y}$ is the network output. To capture the dynamics in the system we use internal feed-back units. The weights in network f are then adjusted so that the error between the desired output y and the network output $\hat{y}$ is minimised. The desired output is the normalised $\log r$ according to

$$y = \frac{\log r - \alpha}{\beta}. \tag{23}$$

The normalising constants are for the four different models are shown in the table below.

Table 1: The normalising constants for the four models.

Model	α	β
BFE ΔX	0.064	1.2
BFE ΔY	-0.0079	1.2
UPS ΔX	0.020	1.4
UPS ΔY	-0.062	1.3

4.4   Training and optimisation

The solar wind data and ground magnetic field data are extracted from the five year period 1998–2003. Only events during which $r(t)$ reach above a certain threshold are selected, and all the events are sorted in r. Then the set is split into three independent data sets by selecting every third event. This results in about $15\,000$ data points in each set, and where each set has similar mean and standard deviation. The three sets are used for training, validation, and testing. The training set is used for the weight adjustment, the validation set is used to determine the optimal network, and the test set is used to test the network. The input data are normalized to cover approximately the range ± 1 and the output is log-normalized. The neural network can be summarized as

$$\overline{\log r_i}(t + \tau) = f_i(\mathbf{x}(t)) \tag{24}$$

where $\overline{\log r_i}$ is the output and τ is the prediction horizon. The goal of the training procedure is to the change the free parameters (weights) of f so that the squared error $(\log r_i(t) - \overline{\log r_i}(t))^2$ is minimized. The network function f contains input units, hidden units, context units, and an output unit. The units are connected with weights, and each hidden and output unit has a bias. The context units contain a delayed copy of the hidden units that are fed back into the hidden units; this is the recurrent layer. To a first approximation, the recurrent layer is an exponential trace memory, where the weights represents the decay terms. Thus, the context units contain the memory of the system.

The weights are initialised to small random values and then the network is trained. Typically, both the training set error and the validation set error decrease during the first part of the training phase as the network adjusts to general features in the data. Then, as training continues the training error still decreases, while the validation error may occasionally increase passing through several local minima. Finally, the validation error just continues to grow while the training error still decreases. The values of the weights at which the network reached the deepest validation minimum is considered to be the optimal weights. During the first phase the network adjusts to general features in the data, then it picks out more detailed features but also starts to adjust to the noise in the data, and then finally the network continues to adjust to the remaining noise. By monitoring the progress of the validation set error we can thus find the optimal network.

A large number of networks with different architectures are trained to predict $\log r_i$, and the optimal network is determined using the validation set. The initial network is fully connected and has 10 inputs, n_h hidden units, $n_c = n_h$ context units, and one output. As the output unit and each hidden unit also has a bias the total number of weights is $n = 10n_h + n_h + n_c n_h + n_h + 1 = 1 + 12n_h + n_h^2$. The number of hidden units is varied over $n_h = 2, 3, 4, 5, 6$ giving networks with $n = 29, 46, 65, 86, 109$ weights.

Starting with the model for the RMS ΔX at Uppsala we see that the maximum correlation is obtained for a network with $n_h = 5$ hidden units (Figure 9, upper left plot). The confidence limits are shown at the 95% level. In computing the correlation and confidence limits we use all three data sets: training set, validation set, and test set. There are almost 40 000 data points but the autocorrelation in both the observed series and the predicted series do not fall off to zero quickly. Therefore the effective number of independent observations (*Quenouille*, 1952; *von Storch and Zwiers*, 1999) is reduced by a factor of about 35 giving slightly more than 1000 independent points. In Figure 9 the horizontal line indicates the level at which the correlation is significantly lower than the highest correlation. This means that all models with a correlation above the line perform equally well, but any model falling below the line performs significantly poorer. Thus, it can be seen that there is a significant increase in the correlation going from 2 hidden units to 3 hidden units, and increasing the number of hidden units has very little (or no) effect. Similar results are obtained for UPS ΔY, and BFE ΔX and ΔY.

4.5 Pruning

It is interesting to see which inputs that have an influence on the model. It is not possible to merely look at the strengths of the weights to judge which inputs are of importance. Instead each weight must be removed and the change in performance monitored. For large networks there are more efficient ways to achieve this in which the second derivative of the error with respect to the weights are computed *Le Cun et al.* (1990). But as the network used here is quite small we may simply remove one input at a time and compute the change in error. Before the error is computed the network is additionally trained for a few iterations so that the remaining weights may be altered to compensate for a possible change in bias. The initial network is fully connected with 10 inputs and 5 hidden units. When one input is removed the total number of weights is decreased by 5. After removing one input at a time we will have a set of 10 different models each having 9 inputs. The model with the highest correlation is chosen from the set to be used for continued pruning. The process is repeated until there is only one input unit left. The network pruning results in the change in correlation according to the points connected with dashed lines in Figure 9. Each label indicate which input that has been removed. The procedure is repeated for Uppsala ΔY, and Brorfelde ΔX and ΔY. For all models the following inputs have no influence: sine and cosine of the year, standard deviations of B_z and velocity V, and density n. Then there are some differences between the models. In both Uppsala and Brorfelde the ΔX-models show a weak dependence on the cosine local time (CLT). Looking at the local time distribution of ΔX it follows a cosine function with a maximum around noon and a minimum around midnight . Further pruning reveals that the most important inputs, ordered in increasing importance, are B_z, σ_n, and V. Now studying the ΔY-models we note that there is a weak coupling to sine local time instead of cosine. Again, looking at the local time distribution there is a maximum in the morning sector that can be described by a sine curve, however, the distribution in the afternoon sector does not follow the sine shape, instead it levels out showing no variation in local time. Ordering the remaining inputs in increasing importance we find σ_n, V, and B_z. Apart from the difference in local time distribution, there also seems to be a difference in the coupling to the solar wind between ΔX and ΔY. The two most important parameters for ΔX are V and σ_n, and they are related to pressure variations in the solar wind that compress the dayside magnetopause. This is also consistent with the local time variation seen in ΔX. On the other hand, for ΔY the two most important parameters are B_z and V that may be interpreted to be more linked to the reconnection process at the magnetopause causing sub-storms and storms.

4.6 Increasing the prediction horizon

As previously mentioned the prediction lead time is 30 minutes. We may examine if it is possible to increase the lead time without degrading the performance of the model. We increase the lead time in steps, with continued training of the network, and compute the correlation. It turns out that the correlation for both ΔX and ΔY monotonically decreases, even though we may extend the lead time to 70-90 minutes before it becomes significantly poorer. However, the ΔX-model shows a steeper decrease in correlation than the ΔY-model. This is consistent with the finding above that solar wind pressure variations are more important for ΔX than ΔY, and that the substorm process dominates the ΔY variations. The magnetopause current responds directly

to solar wind pressure changes so the only available lead time is the L1–Earth travel time. On the other hand there is additional time delays before the substorm develops after the southward turning of B_z.

4.7   Generalisation to interpolated RMS ΔX and RMS ΔY

Models have been developed that predicts the RMS ΔX and RMS ΔY at BFE (Brorfelde) and UPS (Uppsala). However, for the general situation we should be able to predict the RMS values for any location in South Sweden. This can be obtained by developing similar models but that includes the longitude and latitude at the input, and using the RMS of computed interpolated magnetic field as the target output. However, in this work we choose a slightly simpler approach.

Studying the spatial variation of interpolated RMS ΔX and RMS ΔY during the 24-25 September 1998 events it is seen that at any given instant of time the values lie on a rather smooth surface. Assuming a certain shape of the surface, so that it can be described with two parameters, then the values at BFE and UPS can be used to determine the two parameters. We apply principal components analysis (PCA) (*Jolliffe*, 2002) on the interpolated RMS data. Using only the first principal component (PC) 96% of the variance in RMS ΔX is captured, and with two PCs more than 99 % of the variance is captured. For RMS ΔY the 1st PC captures more than 98% of the variance, and the first two PCs more than 99% of the variance.

To conclude, it is thus possible to a high degree of accuracy to compute the 10-minute RMS ΔX and RMS ΔY at any location in the grid using only data from BFE and UPS. Therefore, the forecast models developed for BFE and UPS can be applied also for the locations in the grid.

5   Forecasting GIC

5.1   Single site empirical model from RMS ΔX and RMS ΔY

The GIC flowing between the transformer neutral and the ground has been measured at a location in South Sweden. The measurements have been carried out for a number of periods during the years 1998 to 2000 and the data set consists of almost 100 000 one minute samples *Kronfeldt* (2002). The measured GIC ranges from -269 A to 195 A. As previously stated, with knowledge about the power grid layout and the ground conductivity the GIC may be computed from the time derivative of the horizontal magnetic field *Viljanen et al.* (2003). Therefore, we expect to find a correlation between the MS ΔX and ΔY (r^2), and the MS GIC (g^2). Using a least squares fit between r^2 and g^2 we find

$$\hat{g}^2 = 0.47 + 0.15r_1^2 + 0.08r_2^2 + 0.15r_3^2 + 0.05r_4^2 \; A^2, \tag{25}$$

where $r_1 = \text{RMS}(\Delta X_{BFE})$, $r_2 = \text{RMS}(\Delta Y_{BFE})$, $r_3 = \text{RMS}(\Delta X_{UPS})$, and $r_4 = \text{RMS}(\Delta Y_{UPS})$. The correlation between g^2 and $\hat{g}^2$ is 0.929 ± 0.015 at the 95% confidence level, taking into account the autocorrelation in the time series (*Quenouille*, 1952; *von Storch and Zwiers*, 1999).

In Figure 11 the RMS GIC from the linear model is plotted against the measured RMS GIC. The high correlation of the single site empirical linear model indicates that it should be possible to compute the RMS GIC at other locations and for other power grid configurations using the RMS ΔX and ΔY as inputs.

5.2 General model from interpolated RMS ΔX and ΔY

[Text to be added.]
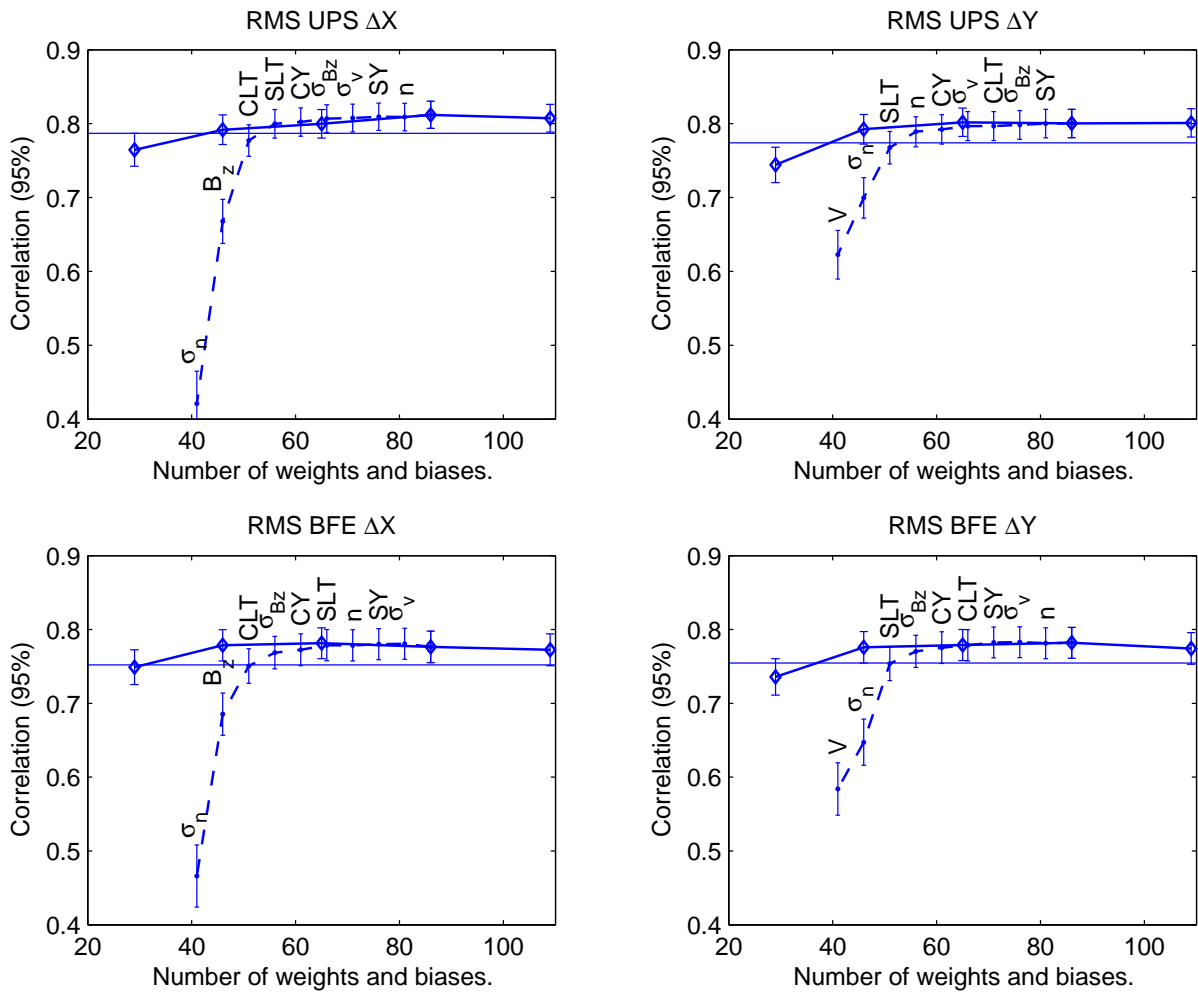
6 Example predictions

[Text to be added.]

Figure 9: The figure shows the correlation coefficients $C(\log r, \overline{\log r})$ for networks with different number of weights and biases. The error bars indicates the 95% confidence levels. The solid curve connected with diamonds corresponds to the fully connected networks with 2,3,4,5 and 6 hidden units. The labels along the dashed curve show which input that has been removed.
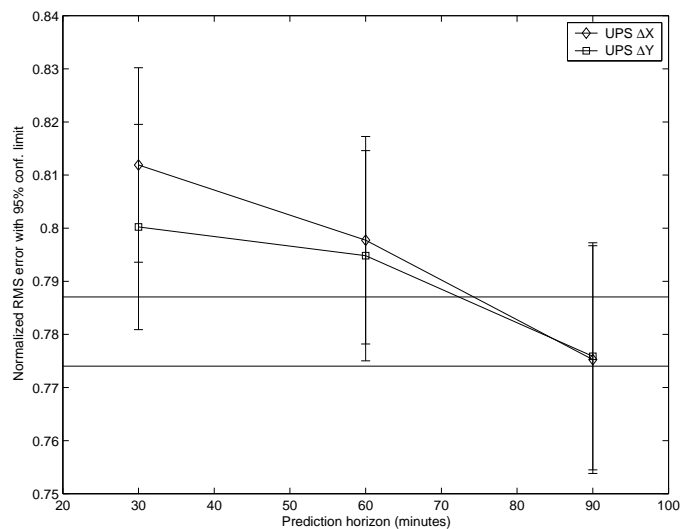
Figure 10: The figure shows the linear correlation between observed and predicted RMS ΔX and RMS ΔY at UPS as a function of prediction lead time. [NB y-axis label is wrong.]
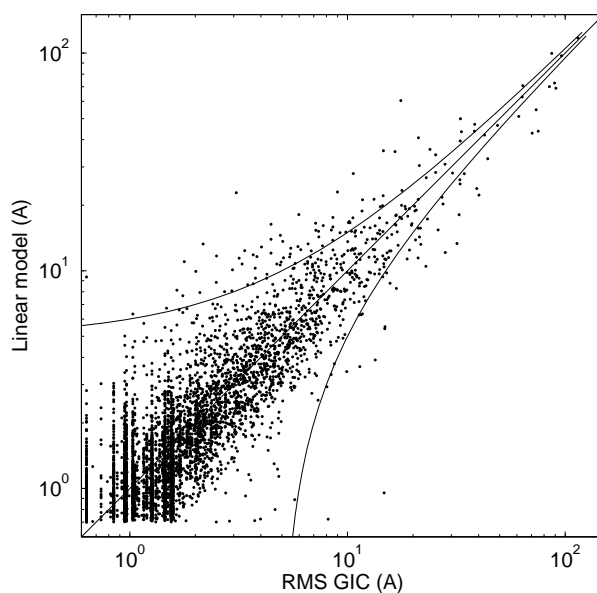

Figure 11: The figure shows a correlation plot between the 10 minute RMS GIC from the linear model and the measured 10 minute RMS GIC. The two curves marks the ± 5 Amp. error.

References

Jolliffe, I. T., *Principal component analysis*, Springer-Verlag, 2002.

Kronfeldt, I., Forecasting and calculating geomagnetically induced currents, 2002.

Le Cun, Y., J. Denker, and S. Solla, Optimal brain damage, in *Neural information processing systems*, vol. 2, edited by D. S. Touretzky, pp. 598–605, Morgan Kaufmann, San Mateo, Denver, 1990.

Percival, D. B., and A. T. Walden, *Wavelet methods for time series analysis*, Cambridge University Press, 2002.

Quenouille, M. H., *Assoicated measurements*, Butterworths Scientific Publications, 1952.

Viljanen, A., A. Pulkkinen, O. Amm, R. Pirjola, T. Korja, and BEAR Working Group, Fast computation of the geoelctric field using the method of elementary current systems and planar earth models, *Annales Geophysicae*, *21*, 1–13, 2003.

Viljanen, A., R. Pirjola, and A. Pulkkinen, Computation of gic from the geomagnetic field, technical note, wp 300, *Tech. rep.*, Finnish Meteorological Institute, P.O.B. 503, FIN-00101 Helsinki, Finland, 2005.

von Storch, H., and F. W. Zwiers, *Statistical analysis in climate research*, Cambridge University Press, 1999.

Weigel, R. S., D. Vassiliadis, and A. J. Klimas, Coupling of the solar wind to temporal fluctuations in ground magnetic fields, *Geophysical Research Letters*, *29*(19), doi: 10.1029/2002GL014740, 2002.

Wintoft, P., H. Lundstedt, and R. Pirjola, A space weather forecast system for geomagnetically induced currents, User Requirements Document, *Tech. rep.*, Swedish Institute of Space Physics, Scheelevgen 17, SE-223 70 Lund, Sweden, 2003.

Wintoft, P., A. Pulkkinen, M. Wik, A. Viljanen, R. Pirjola, H. Lundstedt, and L. Eliasson, Real-time forecast service for geomagnetically induced currents technical note 1: Database, 2004.